Advanced Optical Materials

ADVANCED OPTICAL MATERIALS
www.advopticalmat.de

RESEARCH ARTICLE OPEN ACCESS

Orthogonal Quintuple-Stimuli Responsiveness in an Ultrastable, Ultrabright Cu_{16} Nanocluster via Molecular and Supramolecular Engineering

Leon Li-Min Zhang[1] | Boyang Fu[2] | Weizhao Cai[2] | Min Wu[3] | Kai Wang[3] | Jie Han[4] | Lawrence Yoon Suk Lee[1] | Wai-Yeung Wong[1]

[1]Department of Applied Biology and Chemical Technology & Research Institute for Smart Energy, The Hong Kong Polytechnic University, Hong Kong, P. R. China | [2]School of Materials and Energy, University of Electronic Science and Technology of China, Chengdu, P. R. China | [3]Shandong Key Laboratory of Optical Communication Science and Technology, School of Physics Science and Information Technology, Liaocheng University, Liaocheng, P. R. China | [4]School of Science and Technology, Hong Kong Metropolitan University, Hong Kong, P. R. China

Correspondence: Weizhao Cai (wzhcai@uestc.edu.cn) | Lawrence Yoon Suk Lee (lawrence.ys.lee@polyu.edu.hk) | Wai-Yeung Wong (wai-yeung.wong@polyu.edu.hk)

Received: 5 December 2025 | **Revised:** 23 January 2026 | **Accepted:** 26 January 2026

Keywords: atomically precise clusters | luminescence | multifunctionality | responsive mechanism | stimuli-responsive materials | structure–property relationships

ABSTRACT

The development of high-performance, universal stimuli-responsive materials is hindered by the disconnect between fundamental design principles and macroscopic multifunctionality. Herein, we report an atomically precise copper nanocluster **Cu_{16}**, engineered with the dual alkynyl/perfluorocarboxylate ligands to simultaneously control molecular and supramolecular assembly. Endowed with ambient ultrastability and ultrabright luminescence, **Cu_{16}** undergoes well-defined, stimuli-induced changes that produce distinct, high-contrast responses to five functionally independent stimuli. Systematic studies reveal that **Cu_{16}** operates through a dual-channel responsive mechanism, where the structural channel governs responses to volatile organic compounds and pressure via structural perturbations at different extents, and the luminescent channel mediates responses to temperature, O_2, and X-ray radiation via distinct electronic state transitions. The orthogonal discrimination of five stimuli yields quintuple optical switching effects, which not only establishes **Cu_{16}** as a state-of-the-art stimuli-responsive metal cluster with multidimensional signaling capability, but also confers unprecedented functional breadth. This work provides an atomic-precision blueprint to engineer advanced stimuli-responsive materials with multifunctionality, revealing explicit synthesis–structure–property correlations to guide the development of next-generation programmable smart materials.

1 | Introduction

Stimuli-responsive materials transcend static systems by exhibiting distinct, sensitive, and visually discernible responses to environmental triggers [1–4]. They demonstrate multifunctionality to enable frontier applications in sensing, optoelectronics, anti-counterfeiting, and information storage [5–13]. However, their widespread adoption faces three critical barriers: i) Existing paradigms lack construction principles to create orthogonal activation pathways that ensure stimuli compatibility [14], limiting responses to only 2 – 3 stimuli. Furthermore, when exposed to different stimuli, they exhibit a monotonic optical switching effect—such as simple emission color changes—rather than discriminative optical modulation [15]. To date, integrating a variety

of stimuli into a single material to achieve independent, high-contrast optical responses remains a fundamental challenge, whose resolution would unlock the advanced multidimensional signaling capability [16–18]. ii) While high luminescence quantum yields (QYs) and robust stability are essential for practical applications, existing stimuli-responsive materials typically suffer from insufficient stability and low QYs (< 20%), which diminish visual contrast, reduce sensitivity, and compromise real-world applicability [11, 12, 15]. iii) There is a lack of benchmark studies utilizing structurally precise models to directly link material engineering to the multidimensional signaling performance, impeding the understanding of structure–property correlations to achieve mechanistic progress [3, 4, 11].

Ligand-protected coinage-metal (Cu^I, Ag^I, Au^I) nanoclusters (NCs) constitute a promising platform to overcome these limitations [19–23]. They exhibit molecule-like properties to facilitate tunable photophysics [24–26], offering intrinsic pathways to stimuli responsiveness. Meanwhile, by bridging single atoms and nanoparticles, they possess monodisperse structures that can be characterized at atomic precision, providing unambiguous insights into the stimulus–responsiveness relationships [27–44]. However, their vast structural variability complicates rational design [45–47]. Among the coinage triad, Cu^I NCs underperform their Ag^I and Au^I counterparts [47]. This gap arises from copper's inherent limitations: weak spin-orbit coupling (SOC) and diminished relativistic effects [29, 35, 46], and the oxidation susceptibility of Cu^I due to its low reduction potential [27, 43]. Intuitively, engineering high-performance stimuli-responsive Cu^I NCs is a formidable task. To address this, we revisited the synthetic strategy, focusing on achieving structural control to tailor the luminescent properties.

At the molecular level, ligands critically determine the structures and photophysical properties of metal NCs [26, 47]. While thiolates, selenolates, phosphines, hydrides, alkynyls, and halides with varied donors (S, Se, P, C, and halide) have been frequently employed [29–44], introducing other strongly bound ligands with distinct coordination motifs can assemble novel NCs. This offers dual benefits: enhancing stability by shielding the Cu^I core from the environment [37], and bringing in new luminescent attributes, irrespective of the emission origin (core- or ligand-based) [26]. Supramolecular assembly represents a higher-order approach to tailor luminescence, where the ligand-mediated inter-NC interactions can suppress vibrational non-radiative pathways to enhance QYs [48]. However, achieving controlled supramolecular assembly presents significant challenges, including constructing suitable NC synthons, selecting effective interactions, and controlling subtle assembly parameters [49]. In this context, an innovative ligand strategy that simultaneously controls molecular structure and orchestrates supramolecular organization is essential to achieve stable, high-QY Cu^I NCs [48, 50–53]. Such stability permits well-defined, stimuli-induced transformations for structural analysis, while high QYs enable reliable luminescence tracking, both crucial for mechanistic elucidation of stimuli-responsive behaviors.

Herein, we developed a dual-ligand strategy to realize simultaneous molecular and supramolecular engineering of an atomically precise NC **Cu_{16}**, exhibiting three synergistic features: i) Ultrabright luminescence. Perfluorocarboxylates (O-donor) combine with alkynyls as structural modifiers to assemble **Cu_{16}** as a novel NC luminophore. Concurrently, the dual ligands form a dense 3D supramolecular network, dominated by C—H—F and C—F—F interactions, connecting each NC to twelve neighbors. This rigid matrix suppresses non-radiative decays to achieve a 75.7% QY, the highest reported for Cu^I NCs. ii) Ambient ultrastability. Perfluorocarboxylates impart surface superhydrophobicity, endowing **Cu_{16}** with ambient ultrastability. This ligand strategy provides a direct approach to access ultrastable metal NCs for functional studies. iii) Orthogonal quintuple-stimuli responsiveness. Capitalizing on the high QY and exceptional stability, we studied the responses of **Cu_{16}** to five functionally independent stimuli. Briefly, external stimuli activate the dual structural/luminescent responsive channels, giving rise to quintuple optical switching responses, including thermochromism, luminescence quenching, radioluminescence, photophysical switching, and piezochromism, establishing **Cu_{16}** as a state-of-the-art stimuli-responsive cluster material.

As illustrated in Scheme 1, the luminescent channel mediates responses to temperature, O_2, and X-ray radiation via different electronic state transitions: Temperature drives a dynamic singlet ↔ triplet excited-state switching to induce thermally activated delayed fluorescence (TADF) with thermochromism; Interestingly, O_2 directly harvests the triplet state energy to quench luminescence, simultaneously generating singlet oxygen $^1O_2$; Upon X-ray radiation, **Cu_{16}** generates radioluminescence (RL) via ionization and luminescent decay pathway. By contrast, the responses to VOCs and pressure operate via the structural channel through structural perturbations at different extents: volatile organic compounds (VOCs) trigger single-crystal-to-single-crystal (SCSC) transformations to yield structurally distinct materials to exhibit photophysical switching; Pressure induces a progressive structural evolution (isostructural phase transition → molecular compression → amorphization), leading to a high-contrast piezochromism. Notably, although VOCs and pressure ultimately alter both crystal structure and luminescence, their primary action is to perturb the supramolecular or molecular architecture. These structural changes subsequently modify the electronic environment and energy-transfer pathways, giving rise to the observed luminescence responses. This interplay underscores the interconnected yet functionally separable nature of the two response channels in **Cu_{16}**. This work explored atomic-precision engineering of Cu^I NCs with ambient ultrastability and ultrabright luminescence to enable orthogonal quintuple-stimuli responsiveness with multifunctionality. By establishing deep synthesis–structure–property correlations, we provide a design blueprint for next-generation smart NCs with tailored functionalities.

2 | Results and Discussion

2.1 | Synthesis and Characterization

Cu_{16} was synthesized by reacting $Cu^I{}_2O$, ^{t}BuC≡CH, and C_3F_7COOH in *n*-hexane at 120°C for 10 h. The resulting solution was filtered, and rapid solvent evaporation afforded yellow crystals of **Cu_{16}** in a high yield of 89% (based on Cu). Notably, cooling the filtrate to −20°C instead produced a **Cu_{14}** NC

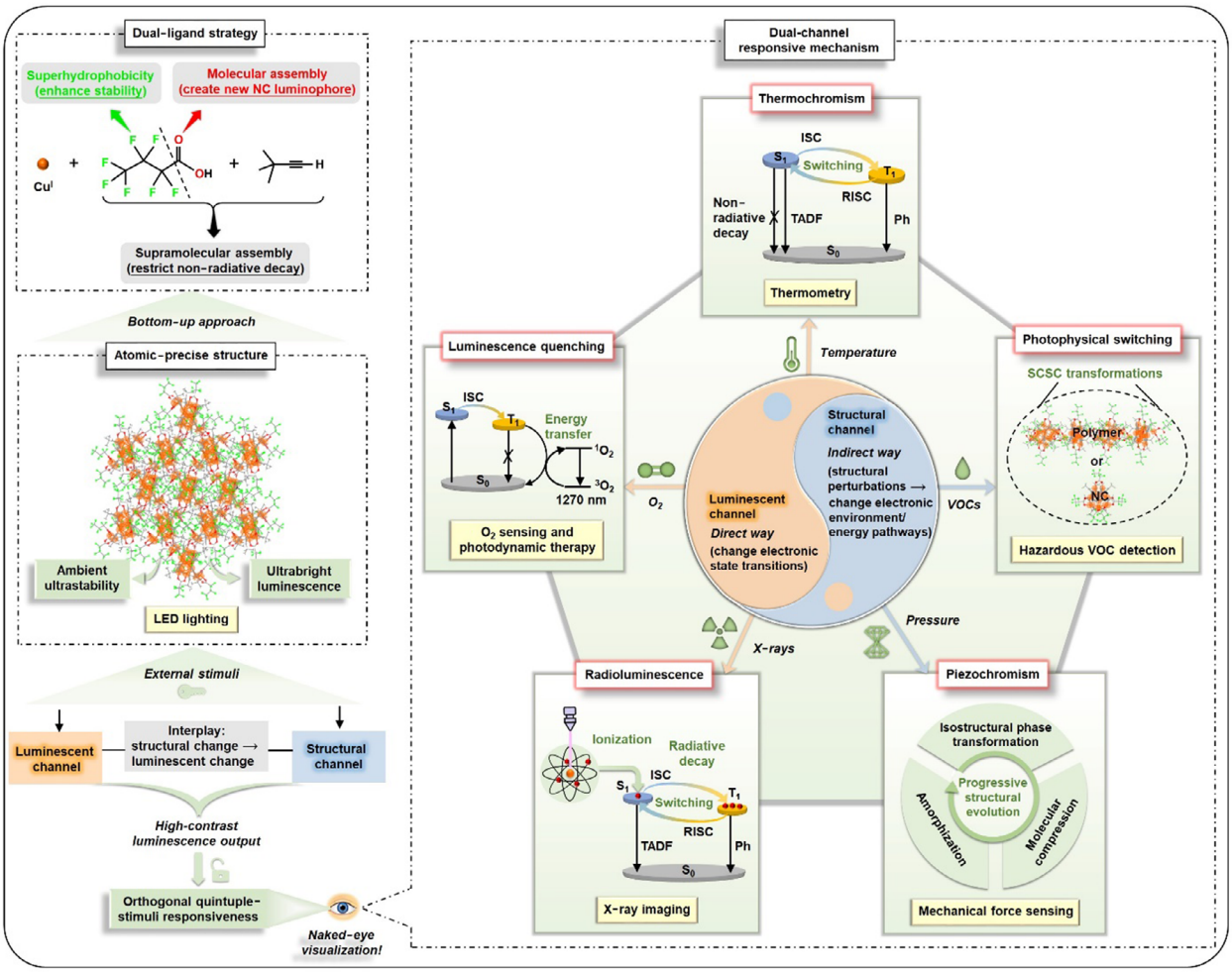

SCHEME 1 | The development of **Cu$_{16}$** that unifies ambient ultrastability, ultrabright luminescence, and orthogonal quintuple-stimuli responsiveness. Abbreviations: NC = nanocluster; QY = quantum yield; LED = light-emitting diode; TADF = thermally activated delayed fluorescence; ISC = intersystem crossing; RISC = reverse intersystem crossing; Ph = phosphorescence; SCSC = single-crystal-to-single-crystal; RL = radioluminescence.

(75% yield). The absence of significant inter-NC interactions in **Cu$_{14}$** gives a low QY of 1.44%, much lower than that of **Cu$_{16}$**. This underscores the crystallization condition as a decisive parameter to steer the assembly of NCs with desirable luminescent properties (see SI for comparison between **Cu$_{14}$** and **Cu$_{16}$**).

Single-crystal X-ray diffraction revealed that **Cu$_{16}$** crystallizes in the $P2_1/c$ space group with a molecular formula $[Cu^{I}_{16}(^{t}BuC{\equiv}C)_8(C_3F_7COO)_8(^{t}BuC{\equiv}CH)_2]$ [54]. The Cu^{I}_{16} kernel can be structurally described as a central Cu^{I}_{12} unit flanked by two Cu^{I}_{2} appendages (Figure 1a), stabilized by two ^{t}BuC≡CH, eight ^{t}BuC≡C^{-}, and eight $C_3F_7COO^{-}$ ligands (Figure S7). To our knowledge, **Cu$_{16}$** represents the first example of a coinage metal NC featuring π-coordinated alkyne → metal bonding [47]. Impressively, the dual $C_3F_7COO^{-}$/^{t}BuC≡C^{-} ligands mediate a dense supramolecular network, linking each NC to twelve neighbors through four interaction types: I) C—H—F, II) C—F—F, III) C—H—H, and IV) C—H—O (Figure 1b), which suppresses the non-radiative decays to boost QY [55]. Hirshfeld surface analysis reveals the relative contributions of interactions I to IV to the total inter-NC contacts as 48.5%, 26.9%, 21.1%, and 2.6%, respectively (Figure 1b).

Beyond supramolecular effect, $C_3F_7COO^{-}$ ligands confer an extreme superhydrophobicity, which is evidenced by a remarkable water contact angle (WCA) of 170.9° (Figure 1c), underpinning the exceptional stability of **Cu$_{16}$** [56]. The stability is demonstrated by **Cu$_{16}$** retaining its crystallinity after one-year ambient storage followed by one-week immersion in aqueous HNO_3 (pH = 1), with its powder X-ray diffraction (PXRD) pattern remaining identical to the simulated pattern. This confirms the robustness of **Cu$_{16}$** against hydrolysis, oxidation, and acidic degradation.

2.2 | Luminescent Property and LED Phosphor

Under UV light excitation at 365 nm, **Cu$_{16}$** exhibits intense yellow emission centered at 587 nm (Figure 2a) with a decay lifetime of 21.0 μs (Figure S16). Its high QY (75.7%) and stability suggest significant potential for solid-state lighting. To demonstrate this utility, a white light-emitting diode (WLED) device was fabricated by coating **Cu$_{16}$** and a green-emitting phosphor $(Ba,Sr)SiO_4:Eu^{2+}$ onto a blue-emitting chip. As displayed in Figure 2b, the device produces white light with CIE (Commission Internationale de l'Éclairage) coordinates of (0.32, 0.33), which are nearly

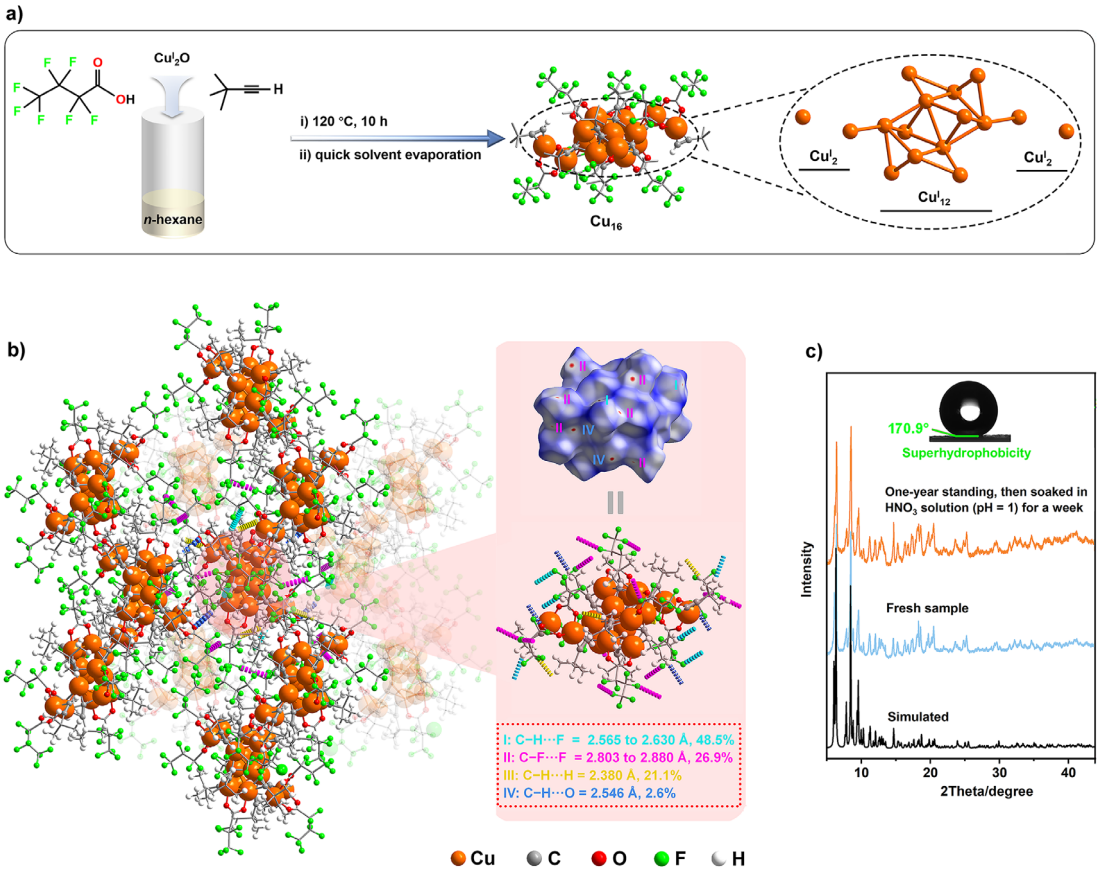

FIGURE 1 | (a) Synthetic route and X-ray structure for **Cu$_{16}$**. Hydrogen atoms of ^{t}Bu groups are omitted for clarity. (b) 3D supramolecular network formed by a NC linking twelve neighbors through four inter-NC interaction types, with their relative contributions calculated by Hirshfeld surface analysis. (c) PXRD patterns of **Cu$_{16}$**. The inset shows the WCA.

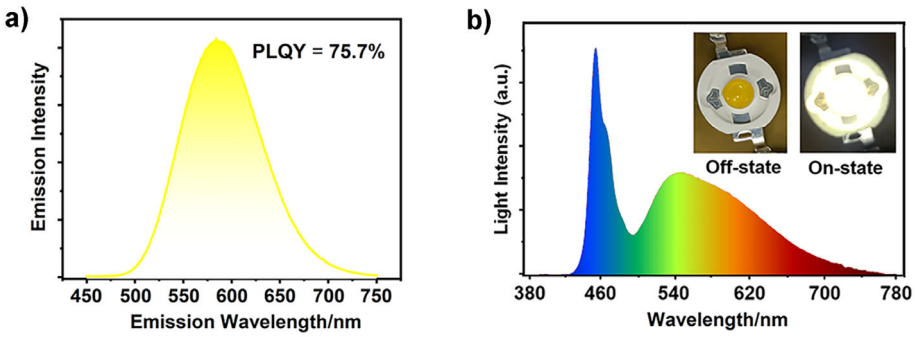

FIGURE 2 | (a) Luminescence spectrum of **Cu$_{16}$** at 298 K. (b) Emission spectrum of the WLED device. Driving current = 20 mA. The inset shows the device in its Off- and On-states.

identical to the ideal white light (0.33, 0.33) [57, 58]. Furthermore, the emission color remains stable under varying driving currents (Figure S18b), confirming **Cu$_{16}$** as a stable phosphor for WLED applications.

2.3 | Thermochromism via TADF

Cu$_{16}$ exhibits TADF arising from dynamic interconversion between singlet (S_1) and triplet (T_1) excited states [59]. This process, sustained by the inter-NC interactions that suppress non-radiative decays, enables its pronounced thermochromism and high QY (Figure 3a). Upon increasing temperature, **Cu$_{16}$** exhibits continuous hypsochromic shifts, transitioning from 626 nm at 9 K to 582 nm at 333 K, accompanied by the luminescent color change from orange-red to yellow (Figure 3b). The emission lifetime evolution reveals distinct regimes (Figure 3c). At 9 – 33 K, the lifetime remains constant at 505 μs, corresponding to the phosphorescence (Ph) regime ($T_1 \rightarrow S_0$). This is followed by a sharp decrease to 80 μs at 203 K, marking the transition from Ph to TADF ($S_1 \rightarrow S_0$) [60]. Upon further warming to 333 K, the lifetime declines to 8 μs without reaching a plateau, indicating

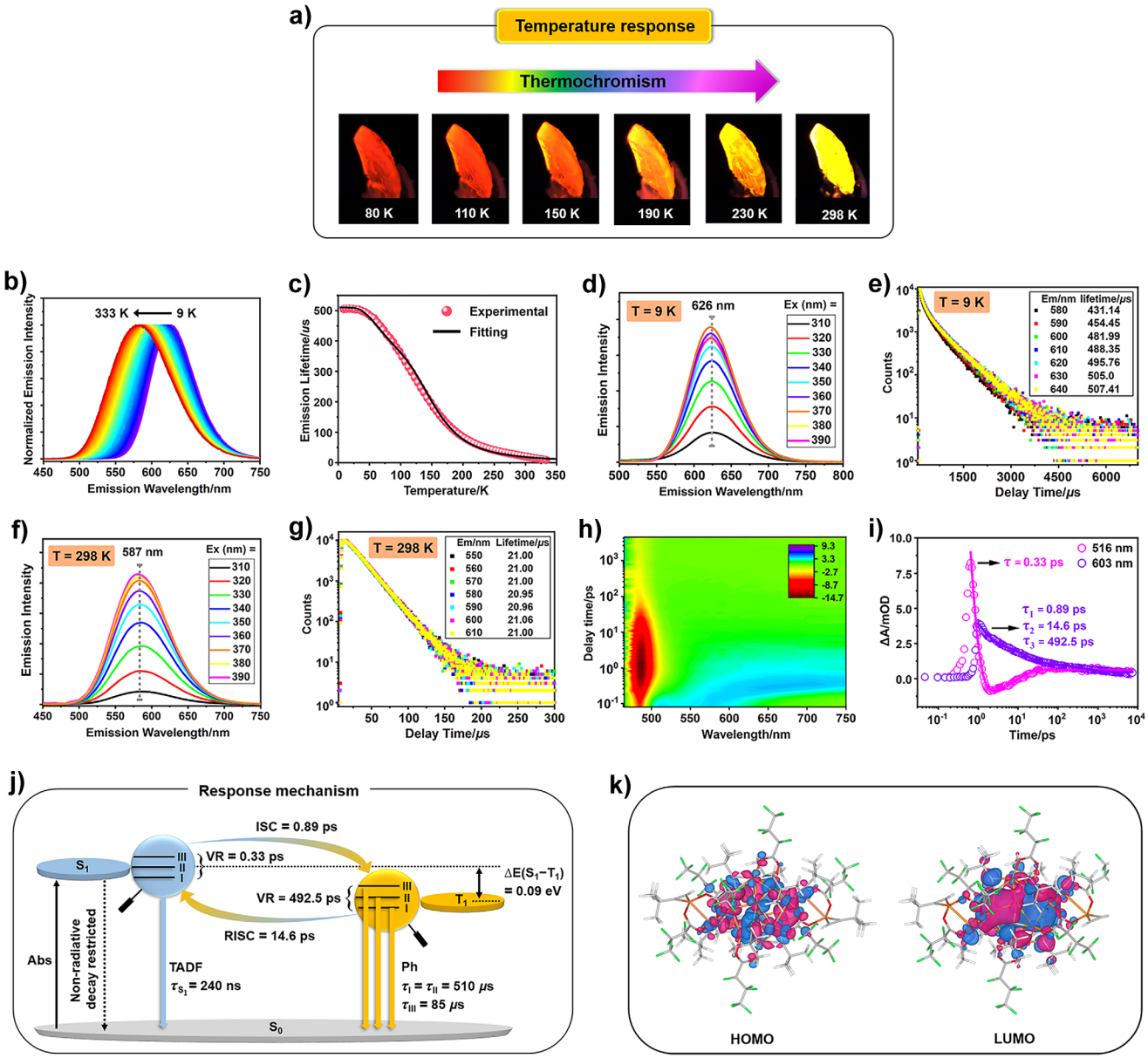

FIGURE 3 | (a) Thermochromic luminescence of $\mathbf{Cu_{16}}$. (b) Temperature-dependent emission spectra. (c) Temperature-dependent lifetimes. The solid line represents the Boltzmann fit. (d–g) Emission spectra under varying excitation wavelengths (d,f) and wavelength-resolved decays (e,g) at 9 and 298 K. (h) 2D contour plot of the ps-ns TA spectra. (i) Kinetic traces (circles) and corresponding fittings (lines) of the ESA peaks. (j) Proposed TADF diagram for $\mathbf{Cu_{16}}$. (k) HOMO and LUMO from TD-DFT calculations.

that a dual TADF/Ph channel is still operating. Fitting lifetimes to the Boltzmann equation [61, 62]:

$$\tau = \frac{1 + e^{-\frac{\Delta E(II-I)}{k_B T}} + e^{-\frac{\Delta E(III-I)}{k_B T}} + e^{-\frac{\Delta E(S_1-T_1)}{k_B T}}}{\tau_I^{-1} + \tau_{II}^{-1} e^{-\frac{\Delta E(II-I)}{k_B T}} + \tau_{III}^{-1} e^{-\frac{\Delta E(III-I)}{k_B T}} + \tau_{S_1}^{-1} e^{-\frac{\Delta E(S_1-T_1)}{k_B T}}}$$

yielded T_1 sublevel splittings $\Delta E(III-I) = 125\ cm^{-1}$ and $\Delta E(II-I) \approx 0$, with lifetimes of $\tau_{III} = 85\ \mu s$ and $\tau_{II} = \tau_I = 510\ \mu s$; the S_1 lifetime, τ_{S1}, is 240 ns; the singlet-triplet splitting energy $\Delta E(S_1-T_1)$ is 0.09 eV, significantly lower than the typical barrier of 0.37 eV required for TADF [61].

The S_1 and T_1 excited states were further characterized. The emission energy at 9 K is independent of the excitation wavelength, revealing that Ph originates solely from the T_1 state (Figure 3d) [63]. The wavelength-resolved lifetimes of 407 to 479 μs prove the existence of T_1 sublevels (Figure 3e) [63, 64]. At 298 K, similarly excitation-independent emission substantiates exclusive S_1 involvement (Figure 3f). While the lifetime remains constant at 21 μs across emission wavelengths (Figure 3g), S_1 sublevels may exist with short lifetimes obscured by Ph. In this vein, picosecond-nanosecond transient absorption (ps-ns TA) spectroscopy resolved the sublevels and excited-state dynamics. A sharp excited-state absorption (ESA) centered at 516 nm decays rapidly ($\tau = 0.33$ ps, Figure 3h,i), attributed to vibrational relaxation (VR) to the lowest-lying S_1 state, verifying the S_1 sublevels. Concurrently, a wide ESA band centered at 603 nm emerges, exhibiting a triexponential decay of 0.89, 14.6, and 492.5 ps, corresponding to ISC, RISC, and VR, respectively (Figure 3i) [45].

The ultrafast $S_1 \rightarrow T_1$ transition occurs in the early time delay of 0.02 – 1 ps, confirming the proposed TADF mechanism [64]. Based on these results, a TADF energy level diagram is proposed in Figure 3j.

Time-dependent density functional theory (TD-DFT) calculations elucidated the electronic origin of **Cu_{16}**. Both S_1 and T_1 states originate primarily from the highest occupied molecular orbital (HOMO) to the lowest unoccupied molecular orbital (LUMO) transition. As shown in Figure 3k, HOMO localizes predominantly on the Cu_{16} kernel with a moderate contribution from ^{t}BuC≡C$^-$, and LUMO is distributed on the Cu_{16} kernel and ^{t}BuC≡C$^-$ ligands. Hence, the emission originates from a Cu_{16} cluster-centered [$d \rightarrow s/p$] transition with partial ligand-to-metal [^{t}BuC≡C$^- \rightarrow s/p$ (Cu)] charge transfer (Table S1). Crucially, the calculated small $\Delta E(S_1-T_1)$ of 0.14 eV and a large spin-orbit coupling (SOC) matrix element of 16.73 cm^{-1} confirm **Cu_{16}** as an effective TADF luminophore, facilitated by rapid RISC [61].

2.4 | O_2-Induced Luminescence Quenching via Energy Transfer

Cu_{16} exhibits O_2-responsive luminescence quenching (Figure 4a,b). The quenching behavior was explored by using the finely ground powder sample to overcome the limited O_2 diffusion inherent to single crystals. Across the full O_2 pressure (PO_2) range of 0 – 101 kPa, the emission quenching ratio (I_0/I) follows an exponential trend (Figure 4c), fitted by the modified Stern-Volmer equation [65, 66]: $I_0/I = 0.06367\exp(0.07801PO_2) + 0.09429$, where I_0 and I represent the emission intensity in vacuum and under O_2, respectively. This nonlinear correlation indicates combined dynamic and static quenching processes, particularly at high O_2 pressures, leading to an amplified quenching effect [66]. At PO_2 = 101 kPa, complete quenching (≈ 99.3%) was achieved. In fact, within the low PO_2 regime of 0 – 21 kPa, quenching is predominantly dynamic, adhering to the linear Stern-Volmer equation: $I_0/I = 0.01079PO_2 + 1$ (K_{sv} = 0.01079 kPa^{-1}) (Figure 4c inset). This exceptionally low quenching constant K_{sv} translates to merely 3% intensity loss at the atmospheric O_2 level (PO_2 = 21 kPa), preserving the bright emission of **Cu_{16}** in air. This contrasts sharply with conventional O_2 sensors that suffer from substantial air quenching [67, 68].

Pressure-dependent lifetime measurements corroborate the dual quenching mechanism (Figure 4d). As shown in Figure 4e, τ_0/τ increases exponentially with PO_2 following $\tau_0/\tau = 3.48\exp(0.016PO_2) - 2.93$ (PO_2 = 0 – 101 kPa), with τ_0 and τ representing the decay lifetime in vacuum and under O_2, respectively. This dependence establishes the coexistence of static and dynamic quenching, since a pure static quenching would not affect the lifetime [67]. Besides, upon switching from vacuum to 101 kPa O_2, the emission vanished within 0.3 s, realizing an in situ real-time quenching (Figure 4f). The quenching reversibility was demonstrated when cycled between vacuum and 101 kPa O_2, maintaining a steady emission-On and -Off response without photobleaching (Figure 4g).

Figure 4h illustrates the quenching mechanism. Following ISC, **Cu_{16}** populates a long-lived triplet excited state. This state transfers energy to the triplet oxygen $^3O_2$ ($^3\Sigma_g$), in situ generating singlet oxygen $^1O_2$ ($^1\Delta_g$) and returning **Cu_{16}** to the ground state to quench luminescence [69, 70]. Control experiments demonstrate that O_2 is the quencher, giving rise to the characteristic Ph of $^1O_2$ peaked at 1270 nm (Figure 4i) [71]. Indeed, this process is thermodynamically favorable as the triplet-state energy of **Cu_{16}** exceeds the $^1O_2$ excitation energy (0.98 eV) [72]. Very importantly, the TADF mechanism enables effective ISC, boosting triplet population to facilitate $^1O_2$ production [73–75]. Remarkably, continuous photoexcitation yields stable $^1O_2$ production for at least 24 h (Figure 4j), verifying **Cu_{16}** as a robust photosensitizer [76]. Collectively, **Cu_{16}** represents the first metal NC to switch emission and $^1O_2$ production on and off quickly, reversibly, and steadily, enabling dual-function oxygen sensing and photodynamic applications.

2.5 | X-Ray-Induced RL via Ionization and Radiative Decay

Upon X-ray irradiation, **Cu_{16}** generates RL with an emission profile identical to its photoluminescence (Figure 5a,d, Figure S29), confirming the same emissive states. Unlike hygroscopic inorganic scintillators that degrade under ambient conditions [77, 78], **Cu_{16}** exhibits persistent RL even after acid treatment (Figure 5b). Furthermore, it functions as a sensitive X-ray dosimeter, exhibiting a linear RL response to the X-ray dose rate in the range of 3.50 – 34.8 μGy s^{-1} (Figure 5c,d). The calculated LOD (limit of detection) is 1.5 μGy s^{-1}, lower than the standard dosage of 5.5 μGy s^{-1} required for X-ray diagnosis [79]. **Cu_{16}** also exhibits excellent radiation stability, as confirmed by continuous radiation over 100 cycles (Figure 5e).

The RL generation mechanism is depicted in Figure 5f. The ionization process initiates when Cu atoms absorb high-energy X-ray photons, ejecting hot electrons via the photoelectric effect [59, 80]. The hot electrons further collide with other atoms of the NCs to produce secondary electrons. After energy dissipation, these electrons are captured by the NCs to form hole-electron pairs, producing S_1 (25%) and T_1 (75%) excitons by obeying the spin-conservation rule [81]. Finally, radiative decay of these excitons via the established luminescent pathway produces RL [82]. Leveraging the persistent RL, a wafer was fabricated from **Cu_{16}** to evaluate its X-ray imaging capability. Using a standard test pattern plate, the wafer demonstrates a high spatial resolution of 20 lp mm^{-1} (Figure 5g). In addition, **Cu_{16}** resolved fine structural details of staples and an integrated circuit chip (Figure 5h,i). These results validate **Cu_{16}** as a novel, stable scintillator for X-ray detection and imaging.

2.6 | VOC-Induced Photophysical Switching via SCSC Transformations

Cu_{16} recognizes six types of hazardous VOCs by exhibiting discernible colorimetric and luminescent responses. Based on their types, they are clarified into: i) aliphatic alcohol; ii) formamides; iii) alkylnitriles; iv) THF; v) arenes and aryl halides; and vi) chloroalkanes (representative examples shown in Figure 6a). Such capability leverages the VOC-specific SCSC transformations (Figure 6e), where upon exposure of **Cu_{16}** to i)–vi), compounds **1–6** were generated correspondingly [54]. **1–6** endow emergent

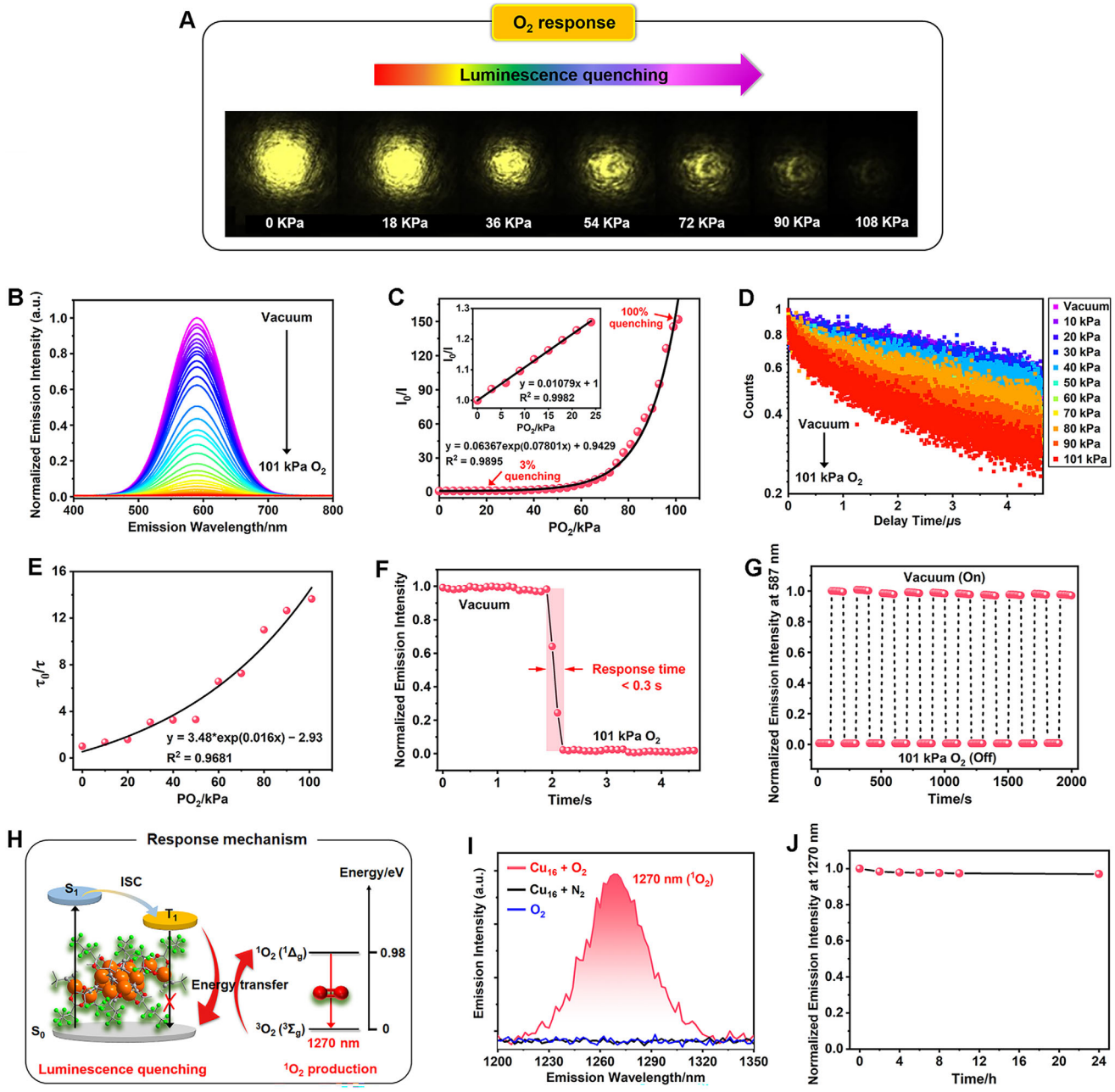

FIGURE 4 | (a) Luminescence quenching of **Cu_{16}**. (b) PO_2-dependent emission spectra. (c) Stern-Volmer plot of I_0/I vs PO_2 across the entire pressure range of PO_2 = 0 – 101 kPa. Inset shows the low-pressure region of PO_2 = 0 – 24 kPa. (d) PO_2-dependent decay spectra. (e) Stern-Volmer plot of τ_0/τ vs PO_2. (f) Transient emission response to O_2. (g) Emission-On and -Off pattern upon vacuum/101 kPa O_2 switching for 10 cycles. (h) Proposed quenching mechanism. (i) NIR emission spectrum of $^1O_2$. (j) Normalized emission intensity at 1270 nm as a function of time.

optical and luminescent properties (Figure 6b,c), thus enabling VOC differentiation via a 2D map based on their bandgap and emission energies (Figure 6d). Particularly, **Cu_{16}** serves as a dual colorimetric-luminescent sensor for type i to iv VOCs.

Remarkably, **Cu_{16}** achieves record-low trace detection of 1-pentanol and DMF (Figure 6e). Exposure to 1-pentanol at a concentration of 6.5 mg/L transformed yellow **Cu_{16}** crystals into red crystals of $[Cu^{I}_{15}(^{t}BuC{\equiv}C)_{10}(C_3F_7COO)_5]$ (**1**), inducing a near-infrared (NIR) emission (peak = 730 nm). Similarly, exposure to DMF at a concentration of 0.5 mg/L yielded orange crystals of $[Cu^{I}_{14}(^{t}BuC{\equiv}C)_{10}(C_3F_7COO)_4(DMF)_2]$ (**2**) with a red emission (peak = 680 nm). These transformations originate from VOC-triggered facile cleavage of the ^{t}BuC≡CH ligand, initiating SCSC processes to generate **1**–**6**. We observed that **Cu_{16}** could not be recovered from **1**–**6** due to the difficulty in reconstituting ^{t}BuC≡CH. Taken together, **Cu_{16}** represents a unique NC platform demonstrating unprecedented structural versatility, from new discrete NCs (**1**–**4**) to NC-based polymers (**5** and **6**), to discriminate a broad spectrum of VOCs, featuring dual colorimetric-luminescent responses, and trace sensing of 1-pentanol and DMF [83–85].

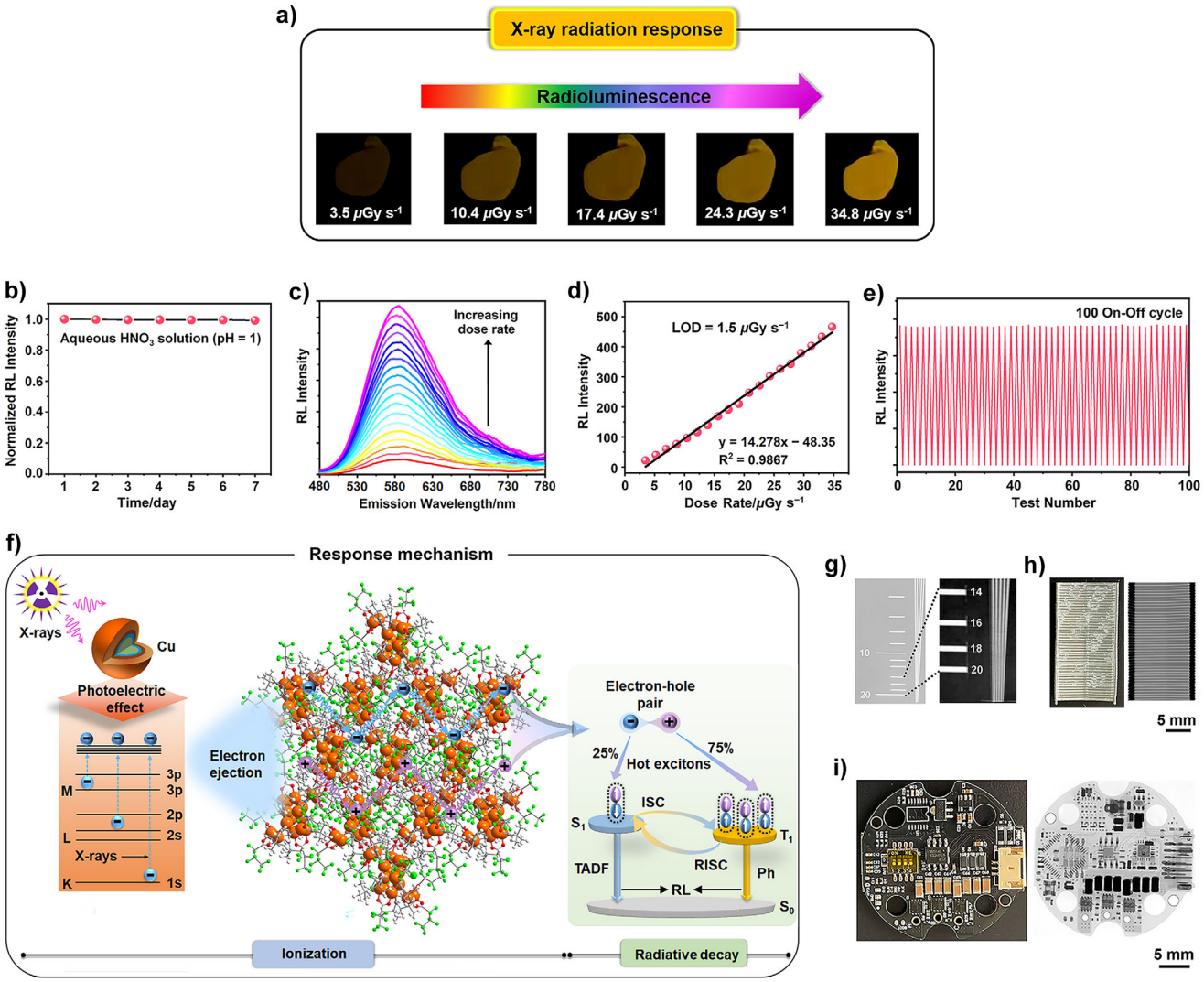

FIGURE 5 | (a) RL of a $\mathbf{Cu_{16}}$ pellet. (b) Persistent RL of $\mathbf{Cu_{16}}$ after one-year ambient storage, followed by one-week acid treatment. (c) RL spectra as a function of dose rate. (d) Fitting of the RL intensity to the dose rate. (e) 100-cycle radiation stability. (f) Proposed mechanism for RL generation. (g) X-ray images of a standard X-ray resolution pattern plate. (h,i) Photographs of staples (h) and an electronic chip (i) under bright-field light (left) and X-ray exposure (right).

2.7 | Pressure-Driven Piezochromism via Progressive Structural Evolution

$\mathbf{Cu_{16}}$ exhibits a high-contrast piezochromic behavior (Figure 7a), which was disclosed by the diamond anvil cell (DAC) device (see Section S7 for instrumental details) [86]. The structural evolution was investigated by synchrotron PXRD. When pressure increases, all Bragg diffraction peaks shift to the higher 2theta angle regions due to crystal lattice contraction (Figure 7b). According to the Le Bail refinement results, the *a*, *b*, and *c* axes are reduced anisotropically by around 12%, resulting in a 30% reduction of the cell volume (Figure 7c). Notably, an isostructural phase transition (phase I → phase II) occurs at around 2 GPa, as evidenced by a discontinuity in lattice constants/volume without the presence of new diffraction peaks [87]. The pressure-volume data were modeled using the second-order and third-order Birch-Murnaghan equation of state, yielding bulk modulus of B_0 = 8.3 GPa for phase I, and B_0 = 31 GPa for phase II (Figure 7c), suggesting significant structural stiffening after transition. Above 10 GPa, all peaks weaken and broaden with an obvious contribution from the background, indicating pressure-induced amorphization under quasi-hydrostatic conditions [88].

This structural evolution drives a pronounced piezochromism. From 1 atm to 15.16 GPa, $\mathbf{Cu_{16}}$ undergoes a drastic optical color change from yellow to dark brown (Figure 7a). This is accompanied by a continuous redshift of the UV–vis absorption edge (Figure 7d), corresponding to a marked reduction of bandgap energy from 2.75 (1 atm) to 1.88 eV (15.16 GPa) (Figure 7e). Notably, the occurrence of phase transition was also observed at around 2.0 GPa, where the decreasing rate of the bandgap energy of 42 meV GPa^{-1} in phase I (1 atm – 2.0 GPa) is slightly smaller than that of 47 meV GPa^{-1} in phase II (2.0 – 15.16 GPa), correlating with the crystallographic phase transition observed by PXRD. Upon releasing pressure to 1 atm (denoted as R1 atm), the initial color of $\mathbf{Cu_{16}}$ could not be reverted (Figure S41). $\mathbf{Cu_{16}}$ also exhibits piezochromic luminescence. With increasing pressure, the emission intensity decreases monotonically until quenching

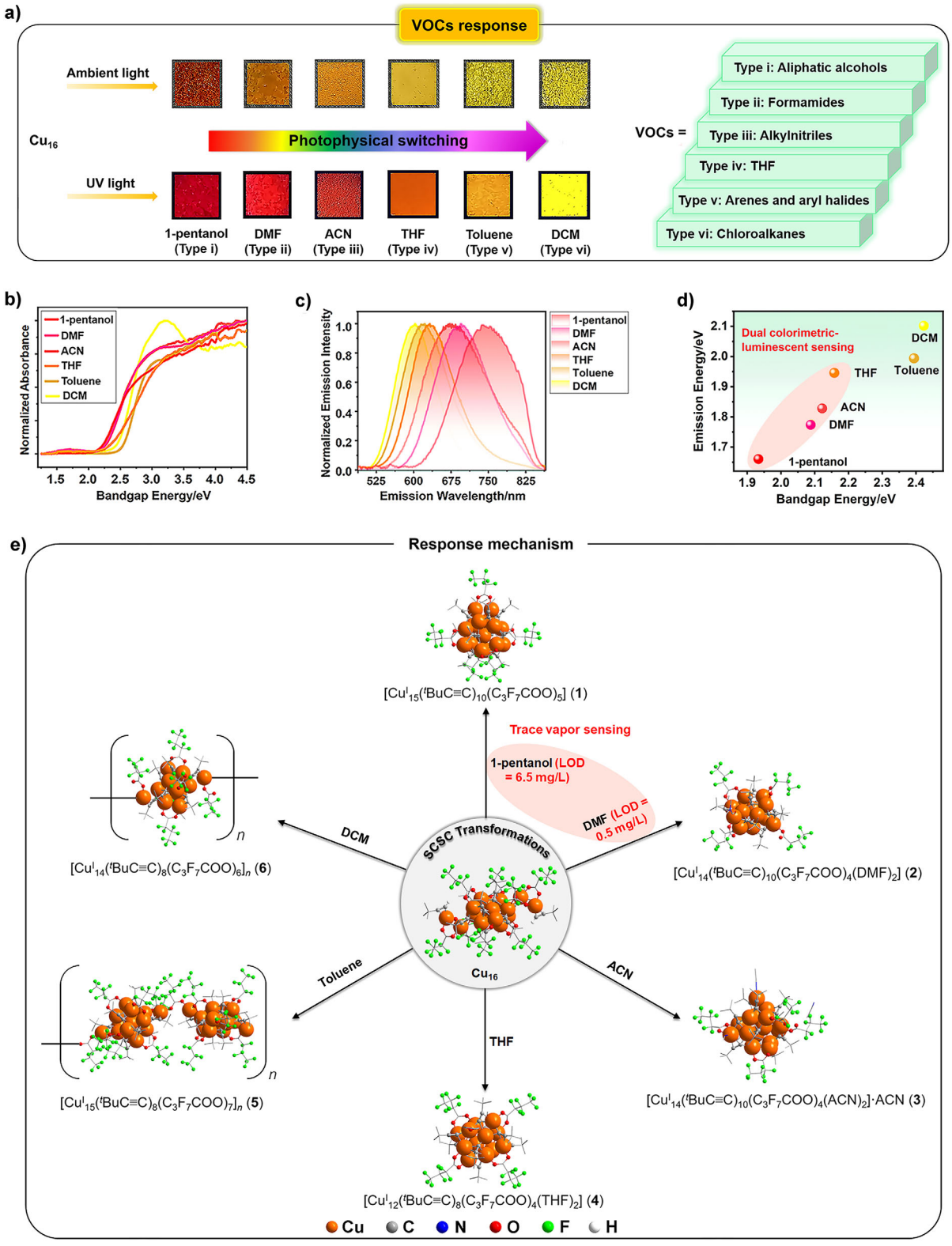

FIGURE 6 | (a) Photophysical switching of **Cu_{16}** upon exposure to type i–iv VOCs, forming six distinct crystalline phases. (b,c) UV–vis diffuse reflectance spectra b) and emission spectra c) of the crystalline products. (d) 2D map based on the bandgap and emission energy of the crystalline products. (e) Crystal structures of products **1**–**6** formed with type i–iv VOCs. Formation of **1** and **2** was achieved at trace amounts of 1-pentanol and DMF, respectively, realizing the trace vapor sensing.

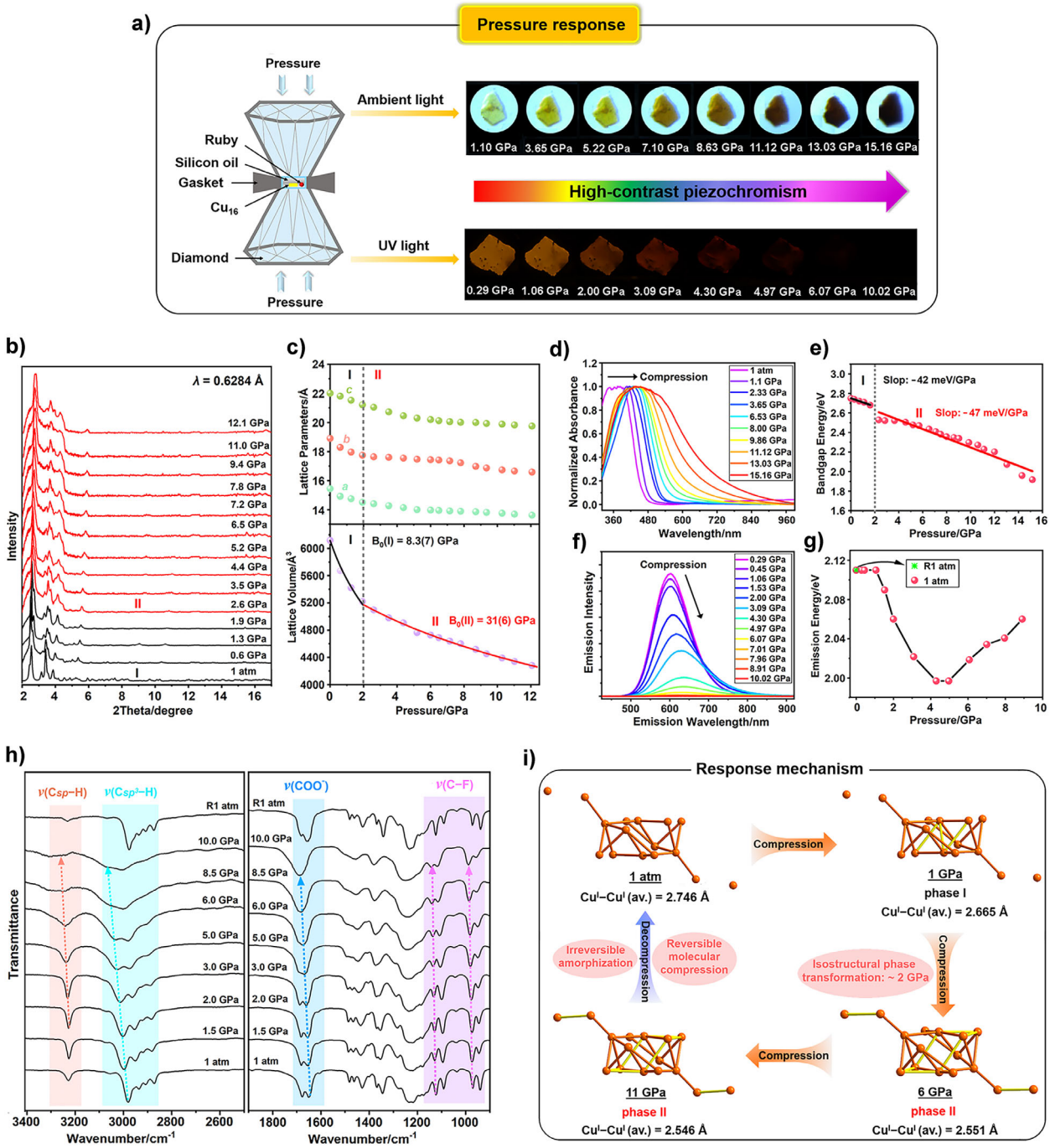

FIGURE 7 | (a) High-contrast piezochromism of $\mathbf{Cu_{16}}$. (b) Evolution of synchrotron PXRD patterns. (c) Evolution of unit-cell volume and lattice parameters. For the volume-pressure data, the black and red solid lines represent the second-order and third-order Birch-Murnaghan fits, respectively. (d,e) Evolution of UV–vis absorption spectra (d) and bandgap energies (e). (f,g) Evolution of emission spectra (f) and emission energies (g,h) Evolution of IR spectra in selected ranges. (i) Proposed mechanism for piezochromism. The Cu^{I}_{16} kernel contraction is simulated by DFT calculations. The pressure-induced short Cu^{I}—Cu^{I} contacts (< 2.8 Å) are highlighted by yellow bonds.

at 10.02 GPa (Figure 7f). The emission peak exhibits an initial redshift followed by a blueshift (Figure 7g). At R1 atm, the peak position recovers but the intensity remains drastically reduced (Figure 7g; Figures S43 and S44), as the amorphization is not fully reversible.

For the infrared (IR) spectra, all peaks shift to the higher frequency regions due to shrinkage of interatomic distances under compression (Figure 7h) [89]. At R1 atm, for C*sp*—H groups without inter-NC interactions, ν(C*sp*—H) restores to the original state at 1 atm, as the molecular compression of $\mathbf{Cu_{16}}$ is reversible (Figure S48). For Csp^3—H, COO^-, and C—F groups involving inter-NC interactions, ν(Csp^3—H), $\nu(COO^-)$, and ν(C—F) could not be fully recovered because these interactions were reorganized by amorphization (Figure S48). DFT calculation results validate the pressure-induced molecular compression, showing

a continuous decrease of the average Cu^{I}—Cu^{I} bond length, denoted as Cu^{I}—Cu^{I} (av.), from 2.746 (1 atm) to 2.546 Å (11 GPa) for the Cu^{I}_{16} kernel (Figure 7i; Figure S46 and S47). This kernel distortion directly drives the bandgap reduction and emission change, as the emission primarily stems from the Cu_{16}-centered transition. Overall, our systematic characterization reveals the high-contrast piezochromism of **Cu_{16}**, stemming from a progressive structural evolution driven by an isostructural phase transition, molecular compression, and a crystalline-to-amorphous state transformation. This work positions **Cu_{16}** as a model system to study the underexplored frontier of piezochromic metal NCs [86, 89, 90].

3 | Conclusions

In summary, we utilized a ligand engineering approach to achieve coordinated molecular/supramolecular control for assembly of an atomically precise **Cu_{16}** NC. This multifaceted platform integrates exceptional intrinsic properties with advanced stimuli-responsive performance. **Cu_{16}** exhibits ambient ultrastability and ultrabright luminescence for practical LED implementation. Upon exposure to five external stimuli, it selectively activates the structural or luminescent response channels in an orthogonal manner to yield five optical switching effects, including thermochromism, luminescence quenching, radioluminescence, photophysical switching, and piezochromism. This responsiveness breadth surpasses all reported responsive materials, which not only provides a platform for selective discrimination of environmental stimuli, but also supports multifunctional applications in temperature/O_2/hazardous VOCs/pressure sensing, photodynamic therapy (via $^1O_2$ generation), and X-ray scintillation imaging. Uniquely, **Cu_{16}** serves as an atomic-precision model system that decodes stimulus–response mechanisms, demonstrating how orthogonal activation pathways can be integrated within a single material to achieve sophisticated multifunctionality. This work significantly deepens the understanding of relationships between nanoscale synthesis, atomic structure, and macroscopic properties at multiple levels, establishing a transformative design-to-function roadmap for next-generation programmable materials.

3.1 | Physical Measurements and Characterizations

Elemental analysis of C and H was carried out on an Agilent 710 Series Inductive Coupled Plasma Optical Emission Spectrometer. Infrared (IR) spectra were recorded on KBr pellets with a Thermo Fisher Scientific Nicolet iS5 spectrometer in the range of 4000 – 400 cm^{-1}. Raman spectra were recorded using a Renishaw Micro-Raman Spectroscopy System equipped with a 785 nm laser source in the range of 4000 – 400 cm^{-1}. Powder X-ray diffraction (PXRD) was performed using a Rigaku SmartLab X-ray diffractometer (CuKα radiation) at a sweeping rate of 5°/min. Thermogravimetric analysis (TGA) was carried out on a Mettler Toledo TGA/DSC 3+ analyzer at a ramp rate of 10°C/min from 40 to 700°C under an N_2 atmosphere. SEM-EDS tests were conducted by a TESCAN VEGA3 scanning electron microscope. UV–vis diffuse reflectance spectra were recorded on a SHIMADZU UV-3600 spectrophotometer using the finely ground samples with $BaSO_4$ reference, and the corresponding bandgap energy was estimated from the *Tauc* plot by using $(\alpha h\nu)^2$ vs. hν. X-ray photoelectron spectroscopy (XPS) and LMM Auger spectra were carried out on a Thermo Scientific K-Alpha spectrometer equipped with a monochromatic Al Kα X-ray source (hν = 1486.6 eV) operating at 150 W and a spot size of 400 μm; survey scans were measured at a constant pass energy of 150 eV and region scans at 50 eV; binding energies were referenced to the C 1*s* peak of the (C—C, C—H) bond, which was set at 284.8 eV. Water contact angle (WCA) was measured on a Lauda Scientific LSA100 instrument (water droplet volume = 5 μL) at room temperature. Thickness of the wafer and pellets was measured on an optical profilometer of Mahr MarSurf LD 130. Transient absorption spectra were recorded on a HARPIA ultrafast transient absorption spectroscopy with a PHAROS laser by using the thin pellets prepared from the samples. Steady-state photoluminescent measurements including PL spectra, lifetime decay, QY, and 3D excitation-emission matrix (3D-EEM) luminescence were conducted on crystal samples using an Edinburgh FLS1000 spectrometer (excitation wavelength = 365 nm); absolute photoluminescence QY was measured with an integrating sphere for six times with a standard deviation of 0.02, with re-absorption/scattering corrected; temperature-dependent study in the range of 9 to 333 K was conducted with the assistance of a liquid helium cryostat; long decay lifetimes in the microsecond scale were measured using μF_2 microsecond flash lamp as the excitation source, and short decay lifetimes in the nanosecond scale were measured using EPL-Series picosecond pulsed diode laser. Photosensitized $^1O_2$ generation was directly monitored by the FLS980 spectrometer with an InGaAs NIR detector under different atmospheres. For stimulus-responsive experiments, complete instrumentation configurations are detailed in their respective sections.

Acknowledgements

The authors gratefully acknowledge the financial support from the RGC Senior Research Fellowship Scheme (SRFS2021-5S01), the Hong Kong Research Grants Council (PolyU 15301922), Research Institute for Smart Energy (CDAQ), Research Centre for Organic Electronics (CE0P), Miss Clarea Au for the Endowed Professorship in Energy (847S), and start-up fund (BE67) from The Hong Kong Polytechnic University. This research is also supported by the National Natural Science Foundation of China (No. 22201237, 12274062 and 12304262).

Conflicts of Interest

There are no conflicts to declare.

Data Availability Statement

The data that support the findings of this study are available in the supplementary material of this article.

References

1. N. Hosono, A. Terashima, S. Kusaka, R. Matsuda, and S. Kitagawa, "Highly Responsive Nature of Porous Coordination Polymer Surfaces Imaged by in Situ Atomic Force Microscopy," *Nature Chemistry* 11 (2019): 109–116.

2. Y. Shen, X. Le, Y. Wu, and T. Chen, "Stimulus-Responsive Polymer Materials Toward Multi-Mode and Multi-Level Information

Anti-Counterfeiting: Recent Advances and Future Challenges," *Chemical Society Reviews* 53 (2024): 606–623.

3. D. Yan, Z. Wang, and Z. Zhang, "Stimuli-Responsive Crystalline Smart Materials: From Rational Design and Fabrication to Applications," *Accounts of Chemical Research* 55 (2022): 1047–1058.

4. N. Li, J. Pang, F. Lang, and X.-H. Bu, "Flexible Metal–Organic Frameworks: From Local Structural Design to Functional Realization," *Accounts of Chemical Research* 57 (2024): 2279.

5. R. Deng, F. Qin, R. Chen, W. Huang, M. Hong, and X. Liu, "Temporal Full-Colour Tuning Through Non-Steady-State Upconversion," *Nature Nanotechnology* 10 (2015): 237–242.

6. L. Pan, S. Sun, A. Zhang, et al., "Truly Fluorescent Excitation-Dependent Carbon Dots and Their Applications in Multicolor Cellular Imaging and Multidimensional Sensing," *Advanced Materials* 27 (2015): 7782–7787.

7. S. Yagai, S. Okamura, Y. Nakano, et al., "Design Amphiphilic Dipolar π-Systems for Stimuli-responsive Luminescent Materials Using Metastable States," *Nature Communications* 5 (2014): 4013.

8. Y. Sagara, and T. Kato, "Mechanically Induced Luminescence Changes in Molecular Assemblies," *Nature Chemistry* 1 (2009): 605–610.

9. T. Kakuta, T.-A. Yamagishi, and T. Ogoshi, "Stimuli-Responsive Supramolecular Assemblies Constructed from Pillar[n]arenes," *Accounts of Chemical Research* 51 (2018): 1656–1666.

10. L. Gu, H. Wu, H. Ma, et al., "Color-Tunable Ultralong Organic Room Temperature Phosphorescence From a Multicomponent Copolymer," *Nature Communications* 11 (2020): 944.

11. Y. Huang, L. Ning, X. Zhang, Q. Zhou, Q. Gong, and Q. Zhang, "Stimuli-Fluorochromic Smart Organic Materials," *Chemical Society Reviews* 53 (2024): 1090–1166.

12. E. Li, K. Jie, M. Liu, X. Sheng, W. Zhu, and F. Huang, "Vapochromic Crystals: Understanding Vapochromism From the Perspective of Crystal Engineering," *Chemical Society Reviews* 49 (2020): 1517–1544.

13. J. Zhuang, M. R. Gordon, J. Ventura, L. Li, and S. Thayumanavan, "Multi-Stimuli Responsive Macromolecules and Their Assemblies," *Chemical Society Reviews* 42 (2013): 7421–7435.

14. Z.-Q. Yao, K. Wang, R. Liu, et al., "Dynamic Full-Color Tuning of Organic Chromophore in a Multi-Stimuli-Responsive 2D Flexible MOF," *Angewandte Chemie International Edition* 61 (2022): 202202073.

15. L. Duan, Q. Zheng, Y. Liang, and T. Tu, "From Simple Probe to Smart Composites: Water-Soluble Pincer Complex With Multi-Stimuli-Responsive Luminescent Behaviors," *Advanced Materials* 36 (2024): 2409620.

16. D. Li, J. Yang, M. Fang, B. Z. Tang, and Z. Li, "Stimulus-responsive Room Temperature Phosphorescence Materials With Full-Color Tunability From Pure Organic Amorphous Polymers," *Science Advances* 8 (2022): abl8392.

17. R.-B. Lin, F. Li, S.-Y. Liu, X.-L. Qi, J.-P. Zhang, and X.-M. Chen, "A Noble-Metal-Free Porous Coordination Framework With Exceptional Sensing Efficiency for Oxygen," *Angewandte Chemie International Edition* 52 (2013): 13429–13433.

18. Y. Zhang, L. Gao, X. Zheng, et al., "Ultraviolet Irradiation-Responsive Dynamic Ultralong Organic Phosphorescence in Polymeric Systems," *Nature Communications* 12 (2021): 2297.

19. M.-L. Fu, I. Issac, D. Fenske, and O. Fuhr, "Metal-Rich Copper Chalcogenide Clusters at the Border Between Molecule and Bulk Phase: The Structures of $[Cu_{93}Se_{42}(SeC_6H_4SMe)_9(PPh_3)_{18}]$, $[Cu_{96}Se_{45}(SeC_6H_4SMe)_6(PPh_3)_{18}]$, and $[Cu_{136}S_{56}(SCH_2C_4H_3O)_{24}(dpppt)_{10}]^+$," *Angewandte Chemie International Edition* 49 (2010): 6899–6903.

20. V. K. Kulkarni, B. N. Khiarak, S. Takano, et al., "N-Heterocyclic Carbene-Stabilized Hydrido Au_{24} Nanoclusters: Synthesis, Structure, and Electrocatalytic Reduction of CO_2," *Journal of the American Chemical Society* 144 (2022): 9000–9006.

21. X. Liu, E. Wang, M. Zhou, et al., "Asymmetrically Doping a Platinum Atom into a Au_{38} Nanocluster for Changing the Electron Configuration and Reactivity in Electrocatalysis," *Angewandte Chemie International Edition* 61 (2022): 202207685.

22. X. Liu, and D. Astruc, "Atomically Precise Copper Nanoclusters and Their Applications," *Coordination Chemistry Reviews* 359 (2018): 112–126.

23. G. Deng, S. Malola, T. Ki, et al., "Structural Isomerism in Bimetallic $Ag_{20}Cu_{12}$ Nanoclusters," *Journal of the American Chemical Society* 146 (2024): 26751–26758.

24. X. Wang, B. Yin, L. Jiang, et al., "Ligand-Protected Metal Nanoclusters as Low-loss, Highly Polarized Emitters for Optical Waveguides," *Science* 381 (2023): 784–790.

25. M. Zhou, T. Higaki, G. Hu, et al., "Three-Orders-of-Magnitude Variation of Carrier Lifetimes With Crystal Phase of Gold Nanoclusters," *Science* 364 (2019): 279–282.

26. Y. Zeng, S. Havenridge, M. Gharib, et al., "Impact of Ligands on Structural and Optical Properties of Ag_{29} Nanoclusters," *Journal of the American Chemical Society* 143 (2021): 9405–9414.

27. X.-Y. Chang, K.-H. Low, J.-Y. Wang, J.-S. Huang, and C.-M. Che, "From Cluster to Polymer: Ligand Cone Angle Controlled Syntheses and Structures of Copper(I) Alkynyl Complexes," *Angewandte Chemie International Edition* 55 (2016): 10312–10316.

28. Z. Luo, X. Yuan, Y. Yu, et al., "From Aggregation-Induced Emission of Au(I)–Thiolate Complexes to Ultrabright Au(0)@Au(I)–Thiolate Core–Shell Nanoclusters," *Journal of the American Chemical Society* 134 (2012): 16662–16670.

29. X.-Y. Xie, P. Xiao, X. Cao, W.-H. Fang, G. Cui, and M. Dolg, "The Origin of the Photoluminescence Enhancement of Gold-Doped Silver Nanoclusters: The Importance of Relativistic Effects and Heteronuclear Gold–Silver Bonds," *Angewandte Chemie International Edition* 57 (2018): 9965–9969.

30. W.-Q. Shi, L. Zeng, R.-L. He, et al., "Near-unity NIR Phosphorescent Quantum Yield From a Room-temperature Solvated Metal Nanocluster," *Science* 383 (2024): 326–330.

31. Q.-H. Wei, L.-Y. Zhang, G.-Q. Yin, L.-X. Shi, and Z.-N. Chen, "Luminescent Heteronuclear $Au^I_5Ag^I_8$ Complexes of $\{1,2,3\text{-}C_6(C_6H_4R\text{-}4)_3\}^{3-}$ (R = H, CH_3, Bu^t) by Cyclotrimerization of Arylacetylides," *Journal of the American Chemical Society* 126 (2004): 9940–9941.

32. J. Yang, R. Pang, D. Song, and M. B. Li, "Tailoring Silver Nanoclusters via Doping: Advances and Opportunities," *Nanoscale Advances* 3 (2021): 2411–2422.

33. A. K. Das, S. Biswas, V. S. Wani, A. S. Nair, B. Pathak, and S. Mandal, "$[Cu_{18}H_3(S\text{-}Adm)_{12}(PPh_3)_4Cl_2]$: Fusion of Platonic and Johnson Solids through a Cu(0) Center and its Photophysical Properties," *Chemical Science* 13 (2022): 7616–7625.

34. X. Liu, G. Saranya, X. Huang, et al., "$Ag_2Au_{50}(PET)_{36}$ Nanocluster: Dimeric Assembly of $Au_{25}(PET)_{18}$ Enabled by Silver Atoms," *Angewandte Chemie International Edition* 59 (2020): 13941–13946.

35. H. Schmidbaur, and A. Schier, "Argentophilic Interactions," *Angewandte Chemie International Edition* 54 (2015): 746–784.

36. J. Chen, P. Gu, G. Ran, et al., "Atomically precise photothermal Nanomachines," *Nature Materials* 23 (2024): 271–280.

37. K. Yonesato, D. Yanai, S. Yamazoe, et al., "Surface-Exposed Silver Nanoclusters Inside Molecular Metal Oxide Cavities," *Nature Chemistry* 15 (2023): 940–947.

38. S. Sharma, K. K. Chakrahari, J. Saillard, and C. W. Liu, "Structurally Precise Dichalcogenolate-Protected Copper and Silver Superatomic Nanoclusters and Their Alloys," *Accounts of Chemical Research* 51 (2018): 2475–2483.

39. S. Lee, M. S. Bootharaju, G. Deng, et al., "$[Cu_{32}(PET)_{24}H_8Cl_2](PPh_4)_2$: A Copper Hydride Nanocluster with a Bisquare Antiprismatic Core," *Journal of the American Chemical Society* 142 (2020): 13974–13981.

40. S. Biswas, A. Pal, M. K. Jena, et al., "Luminescent Hydride-Free $[Cu_7(SC_5H_9)_7(PPh_3)_3$ Nanocluster: Facilitating Highly Selective C–C Bond Formation," *Journal of the American Chemical Society* 146 (2024): 20937–20944.

41. A. W. Cook, Z. R. Jones, G. Wu, S. L. Scott, and T. W. Hayton, "An Organometallic Cu_{20} Nanocluster: Synthesis, Characterization, Immobilization on Silica, and "Click" Chemistry," *Journal of the American Chemical Society* 140 (2018): 394–400.

42. Z. Lei, M. Endo, H. Ube, et al., "N-Heterocyclic Carbene-based C-centered Au(I)-Ag(I) Clusters With Intense Phosphorescence and Organelle-selective Translocation in Cells," *Nature Communications* 13 (2022): 4288.

43. M. Qu, F.-Q. Zhang, D.-H. Wang, H. Li, J.-J. Hou, and X.-M. Zhang, "Observation of Non-FCC Copper in Alkynyl-Protected Cu_{53} Nanoclusters," *Angewandte Chemie International Edition* 59 (2020): 6507–6512.

44. A. Cirri, H. M. Hernández, C. Kmiotek, and C. J. Johnson, "Systematically Tuning the Electronic Structure of Gold Nanoclusters through Ligand Derivatization," *Angewandte Chemie International Edition* 58 (2019): 13818–13822.

45. W. Ishii, Y. Okayasu, Y. Kobayashi, et al., "Excited State Engineering in Ag_{29} Nanocluster Through Peripheral Modification With Silver(I) Complexes for Bright Near-Infrared Photoluminescence," *Journal of the American Chemical Society* 145 (2023): 11236–11244.

46. R. Hamze, J. L. Peltier, D. Sylvinson, et al., "Eliminating Nonradiative Decay in Cu(I) Emitters: >99% Quantum Efficiency and Microsecond Lifetime," *Science* 363 (2019): 601–606.

47. A. Baghdasaryan, and T. Bürgi, "Copper Nanoclusters: Designed Synthesis, Structural Diversity, and Multiplatform Applications," *Nanoscale* 13 (2021): 6283–6340.

48. A. Nag, and T. Pradeep, "Assembling Atomically Precise Noble Metal Nanoclusters Using Supramolecular Interactions," *ACS Nanoscience Au* 2 (2022): 160–178.

49. Z.-H. Zhao, B.-L. Han, H.-F. Su, et al., "Buckling Cluster-Based H-bonded Icosahedral Capsules and Their Propagation to a Robust Zeolite-Like Supramolecular Framework," *Nature Communications* 15 (2024): 9401.

50. K. Pyo, V. D. Thanthirige, K. Kwak, P. Pandurangan, G. Ramakrishna, and D. Lee, "Ultrabright Luminescence From Gold Nanoclusters: Rigidifying the Au(I)–Thiolate Shell," *Journal of the American Chemical Society* 137 (2015): 8244–8250.

51. J. Dong, Z. Gan, W. Gu, et al., "Synthesizing Photoluminescent $Au_{28}(SCH_2Ph\text{-}^tBu)_{22}$ Nanoclusters with Structural Features by Using a Combined Method," *Angewandte Chemie International Edition* 60 (2021): 17932–17936.

52. V. W. W. Yam, V. K. M. Au, and S. Y. L. Leung, "Light-Emitting Self-Assembled Materials Based on d^8 and d^{10} Transition Metal Complexes," *Chemical Reviews* 115 (2015): 7589–7728.

53. C. Heindl, E. V. Peresypkina, A. V. Virovets, W. Kremer, and M. Scheer, "Giant Rugby Ball $[\{Cp^{Bn}Fe(\eta^5\text{-}P_5)\}_{24}Cu_{96}Br_{96}]$ Derived From Pentaphosphaferrocene and $CuBr_2$," *Journal of the American Chemical Society* 137 (2015): 10938–10941.

54. Access Structures, https://www.ccdc.cam.ac.uk/structures.

55. K. G. Liu, X. M. Gao, T. Liu, M. L. Hu, and D. E. Jiang, "All-Carboxylate-Protected Superatomic Silver Nanocluster With an Unprecedented Rhombohedral Ag_8 Core," *Journal of the American Chemical Society* 142 (2020): 16905–16909.

56. L.-H. Xie, M.-M. Xu, X.-M. Liu, M.-J. Zhao, and J.-R. Li, "Hydrophobic Metal–Organic Frameworks: Assessment, Construction, and Diverse Applications," *Advanced Science* 7 (2020): 1901758.

57. Z. Wang, B. Chen, A. S. Susha, et al., "All-Copper Nanocluster Based Down-Conversion White Light-Emitting Devices," *Advanced Science* 3 (2016): 1600182.

58. C. Chen, R.-H. Li, B.-S. Zhu, et al., "Highly Luminescent Inks: Aggregation-Induced Emission of Copper–Iodine Hybrid Clusters," *Angewandte Chemie International Edition* 57 (2018): 7106–7110.

59. P. Yuan, H. Zhang, Y. Zhou, et al., "Thermally Activated Delayed Fluorescence Au-Ag-oxo Nanoclusters: From Photoluminescence to Radioluminescence," *Aggregate* 5 (2024): 475.

60. M. Olaru, E. Rychagova, S. Ketkov, et al., "A Small Cationic Organo–Copper Cluster as Thermally Robust Highly Photo- and Electroluminescent Material," *Journal of the American Chemical Society* 142 (2020): 373–381.

61. T. Hofbeck, U. Monkowius, and H. Yersin, "Highly Efficient Luminescence of Cu(I) Compounds: Thermally Activated Delayed Fluorescence Combined With Short-Lived Phosphorescence," *Journal of the American Chemical Society* 137 (2015): 399–404.

62. T. J. Feuerstein, B. Goswami, P. Rauthe, et al., "Alkali Metal Complexes of an Enantiopure Iminophosphonamide Ligand With Bright Delayed Fluorescence," *Chemical Science* 10 (2019): 4742–4749.

63. Z. Wu, J. Liu, Y. Gao, et al., "Assembly-Induced Enhancement of Cu Nanoclusters Luminescence With Mechanochromic Property," *Journal of the American Chemical Society* 137 (2015): 12906–12913.

64. W.-D. Si, C. Zhang, M. Zhou, et al., "Two Triplet Emitting States in One Emitter: Near-infrared Dual-phosphorescent Au_{20} Nanocluster," *Science Advances* 9 (2023): adg3587.

65. J. Liu, Y. Zhong, P. Lu, et al., "A Superamplification Effect in the Detection of Explosives by a Fluorescent Hyperbranched Poly(silylenephenylene) With Aggregation-enhanced Emission Characteristics," *Polymer Chemistry* 1 (2010): 426–429.

66. D. Genovese, M. Cingolani, E. Rampazzo, L. Prodi, and N. Zaccheroni, "Static Quenching Upon Adduct Formation: A Treatment Without Shortcuts and Approximations," *Chemical Society Reviews* 50 (2021): 8414–8427.

67. R.-W. Huang, Y.-S. Wei, X.-Y. Dong, et al., "Hypersensitive Dual-Function Luminescence Switching of a Silver-Chalcogenolate Cluster-Based Metal–Organic Framework," *Nature Chemistry* 9 (2017): 689–697.

68. Z. Xie, L. Ma, K. E. deKrafft, A. Jin, and W. Lin, "Porous Phosphorescent Coordination Polymers for Oxygen Sensing," *Journal of the American Chemical Society* 132 (2010): 922–923.

69. H. Hirai, S. Takano, T. Nakashima, T. Iwasa, T. Taketsugu, and T. Tsukuda, "Doping-Mediated Energy-Level Engineering of $M@Au_{12}$ Superatoms (M = Pd, Pt, Rh, Ir) for Efficient Photoluminescence and Photocatalysis," *Angewandte Chemie International Edition* 61 (2022): 202207290.

70. W.-J. Guo, Y.-Z. Chen, C.-H. Tung, and L.-Z. Wu, "Ultralong Room-Temperature Phosphorescence of Silicon-Based Pure Organic Crystal for Oxygen Sensing," *CCS Chemistry* 4 (2022): 1007–1015.

71. L. Hou, X. Zhang, T. C. Pijper, W. R. Browne, and B. L. Feringa, "Reversible Photochemical Control of Singlet Oxygen Generation Using Diarylethene Photochromic Switches," *Journal of the American Chemical Society* 136 (2014): 910–913.

72. Y. Song, Y. Li, M. Zhou, et al., "Ultrabright $Au@Cu_{14}$ Nanoclusters: 71.3% Phosphorescence Quantum Yield in Non-Degassed Solution at Room Temperature," *Science Advances* 7 (2021): abd2091.

73. R. Toftegaard, J. Arnbjerg, K. Daasbjerg, et al., "Metal-Enhanced 1270 nm Singlet Oxygen Phosphorescence," *Angewandte Chemie International Edition* 47 (2008): 6025–6027.

74. M. Mitsui, D. Arima, A. Uchida, et al., "Charge-Transfer-Mediated Mechanism Dominates Oxygen Quenching of Ligand-Protected Noble-Metal Cluster Photoluminescence," *The Journal of Physical Chemistry Letters* 13 (2022): 9272–9278.

75. Y.-H. Cheng, A. Belyaev, M.-L. Ho, I. O. Koshevoy, and P.-T. Chou, "The Distinct O_2 Quenching Mechanism Between Fluorescence and Phosphorescence for Dyes Adsorbed on Silica Gel," *Physical Chemistry Chemical Physics* 22 (2020): 27144–27156.

76. Q.-Y. Li, Y.-H. Deng, C. Cao, et al., "Visible Light and Microwave-Mediated Rapid Trapping and Release of Singlet Oxygen Using a Coordination Polymer," *Angewandte Chemie International Edition* 62 (2023): 202306719.

77. X. Fan, F. Yuan, D. Li, et al., "Threefold Collaborative Stabilization of Ag_{14} -Nanorods by Hydrophobic Ti_{16} -Oxo Clusters and Alkynes: Designable Assembly and Solid-State Optical-Limiting Application," *Angewandte Chemie International Edition* 60 (2021): 12949–12954.

78. X. Ou, X. Qin, B. Huang, et al., "High-resolution X-ray Luminescence Extension Imaging," *Nature* 590 (2021): 410–415.

79. R.-W. Huang, X. Song, S. Chen, et al., "Radioluminescent Cu−Au Metal Nanoclusters: Synthesis and Self-Assembly for Efficient Xray Scintillation and Imaging," *Journal of the American Chemical Society* 145 (2023): 13816–13827.

80. W.-F. Wang, M.-J. Xie, P.-K. Wang, et al., "Thermally Activated Delayed Fluorescence (TADF)-Active Coinage-Metal Sulfide Clusters for High-resolution X-ray Imaging," *Angewandte Chemie International Edition* 63 (2024): 202318026.

81. N. Zhang, L. Qu, S. Dai, et al., "Intramolecular Charge Transfer Enables Highly-efficient X-ray Luminescence in Cluster Scintillators," *Nature Communications* 14 (2023): 2901.

82. W. Ma, Y. Su, Q. Zhang, et al., "Thermally Activated Delayed Fluorescence (TADF) Organic Molecules for Efficient X-ray Scintillation and Imaging," *Nature Materials* 21 (2022): 210–216.

83. I. O. Koshevoy, Y.-C. Chang, A. J. Karttunen, M. Haukka, T. Pakkanen, and P.-T. Chou, "Modulation of Metallophilic Bonds: Solvent-Induced Isomerization and Luminescence Vapochromism of a Polymorphic Au–Cu Cluster," *Journal of the American Chemical Society* 134 (2012): 6564–6567.

84. A. Chu, F. K.-W. Hau, L.-Y. Yao, and V. W.-W. Yam, "Decanuclear Gold(I) Sulfido Pseudopolymorphs Displaying Stimuli-Responsive RGBY Luminescence Changes," *ACS Materials Letters* 1 (2019): 277–284.

85. H. Xiang, Y. Wang, X. Xu, et al., "Reversible Interconversion Between Ag_2 and Ag_6 Clusters and Their Responsive Optical Properties," *Journal of the American Chemical Society* 146 (2024): 28572–28579.

86. Q. Li, M. A. Mosquera, L. O. Jones, et al., "Pressure-Induced Optical Transitions in Metal Nanoclusters," *ACS Nano* 14 (2020): 11888–11896.

87. Y. Wang, X. Lü, W. Yang, et al., "Pressure-Induced Phase Transformation, Reversible Amorphization, and Anomalous Visible Light Response in Organolead Bromide Perovskite," *Journal of the American Chemical Society* 137 (2015): 11144–11149.

88. S. Klotz, J. C. Chervin, P. Munsch, and G. L. Marchand, "Hydrostatic Limits of 11 Pressure Transmitting media," *Journal of Physics D: Applied Physics* 42 (2009): 075413.

89. S. Tong, J. Dai, J. Sun, et al., "Fluorescence-based Monitoring of the Pressure-induced Aggregation Microenvironment Evolution for an AIEgen Under Multiple Excitation Channels," *Nature Communications* 13 (2022): 5234.

90. Y. Wang, X. Yang, C. Liu, et al., "Maximized Green Photoluminescence in Tb-Based Metal–Organic Framework via Pressure-Treated Engineering," *Angewandte Chemie International Edition* 61 (2022): 202210836.

Supporting Information

Additional supporting information can be found online in the Supporting Information section.

Supporting File: adom71009-sup-0001-SuppMat.docx.

Supporting File: adom71009-sup-0002-DataFile.zip.